PROCEEDINGS, 44th Workshop on Geothermal Reservoir Engineering
Stanford University, Stanford, California, February 11-13, 2019
SGP-TR-214

Hyperspectral Characterization of Fallon FORGE Well 21-31: New Data and Technology Applications

Kurt O. Kraal and Bridget Ayling

Great Basin Center for Geothermal Energy, University of Nevada, Reno. 1664 N Virginia St, NBMG 0178, Reno, NV 89557

kokraal@nevada.unr.edu, bayling@unr.edu

Keywords: Fallon FORGE, EGS, Infrared Spectroscopy, Hydrothermal Alteration, Hyperspectral, Borehole Geophysics

ABSTRACT

Infrared reflectance spectroscopy is effective at identifying many rock forming minerals, thus it is useful for characterizing lithologies and formations encountered in wells. Characterizing mineralogy and its variability within a formation or with depth can also provide information about past temperatures and rock physical properties that are important for Enhanced or Engineered Geothermal System (EGS) assessment. Advances in hyperspectral imaging technology allow for rapid analyses and the creation of high-resolution mineral maps of geothermal drill core or cuttings samples. This provides the ability to evaluate spatial relationships of minerals within the sample. We performed a new study on core and cuttings from several wells on the Fallon FORGE EGS site using automated high-resolution imaging spectroscopy. Our analysis focuses on well 21-31 that was drilled in early 2018. Spectral maps were acquired using a TerraCore Hyperspectral Core Imaging System (HCIS), with a pixel size of 1.2 mm, equipped with FENIX VNIR-SWIR (400-2500 nm) and OWL LWIR (8-12 μm) cameras, as well as an RGB camera to create a high resolution (0.12 mm pixel size) image of the same drill core or cuttings sample. We interpreted these data for dominant mineralogy, as well as spectral scalars that are related to the mineral structure. In addition, new X-Ray Diffraction (XRD) and thin section analyses were performed on samples from well 21-31 to validate and expand on our hyperspectral interpretation. These data were compared to the extensive existing dataset produced during the Fallon FORGE EGS project, including well log datasets (e.g. temperature and other wireline logs), formation characteristics, and existing mineral and hydrothermal alteration datasets. Finally, we evaluate our data alongside the current conceptual model of the Fallon EGS site.

1. INTRODUCTION

The Frontier Observatory for Research in Geothermal Energy, (FORGE) is an initiative funded by the US Department of Energy that aims to develop the technologies, and knowledge for EGS (Enhanced or Engineered Geothermal Systems) in "hot dry rocks" needed to make EGS commercially viable. The FORGE initiative evaluated several potential sites to host the subsurface FORGE laboratory to test various stimulation approaches in crystalline basement rock formations. The parameters required were a hot impermeable reservoir at depths between 1.5-4 km, with temperatures between 175 and 225 ˚C in crystalline basement rocks. During Phase 1 and Phase 2 of the FORGE project, the Fallon EGS site went through extensive geoscientific characterization to evaluate its suitability as a possible FORGE test site. This research culminated in the drilling of a 2,460 m (8,140 ft) well, 21-31, in February-March 2018. This paper presents some of the new data collected in this well, including mineralogical data derived from rock samples (cuttings and sidewall cores), as well as wireline logs and other borehole geophysical data. In addition, we present new technological applications for infrared spectroscopy to characterize reservoir mineralogy.

Characterization of reservoir mineralogy is important for EGS development for several reasons. First, mineralogy can be useful for understanding the location and character of various lithologies encountered in the wells, particularly in assessing lithologic boundaries and formation correlations between wells. Second, minerals, both primary and secondary, have a strong effect on rock geomechanical properties, such as porosity, permeability, density, and strength (Frolova et al., 2013, Wyering et al., 2014, Mielke et al., 2015). Lastly, understanding the geochemical properties of the reservoir are important for assessing which chemical stimulants and stimulation techniques to use depending on the chemical and mechanical properties of the reservoir.

The primary goals of this study are to characterize the mineralogy and alteration history of well 21-31, to compare the lithological, geochemical, and spectral data with depth to wireline geophysical logs, and compare and assess the strengths and weaknesses of the various methods and sample types.

2. BACKGROUND

2.1 Geologic Background

An extensive dataset was compiled for the Fallon FORGE EGS site during Phase 1 and 2 of the Fallon FORGE project. For a detailed characterization of the geologic framework, see Hinz et al. (2016), Siler et al. (2018), and Faulds et al. (2018). The Fallon site is located in the Carson Sink, a large composite basin in the Basin and Range province. The general stratigraphy of the area is Late-Miocene to Quaternary basin fill sediments (<1.5 km thick), overlying Miocene volcanic rocks (0.7-1.3 km thick), and Mesozoic basement consisting of meta-volcanic and meta-sedimentary rocks that are intruded by felsic plutons. The site is situated in a west-tilted half graben cut by widely spaced northerly striking normal faults with about 200 m of displacement (Siler et al., 2018, Figure 1).

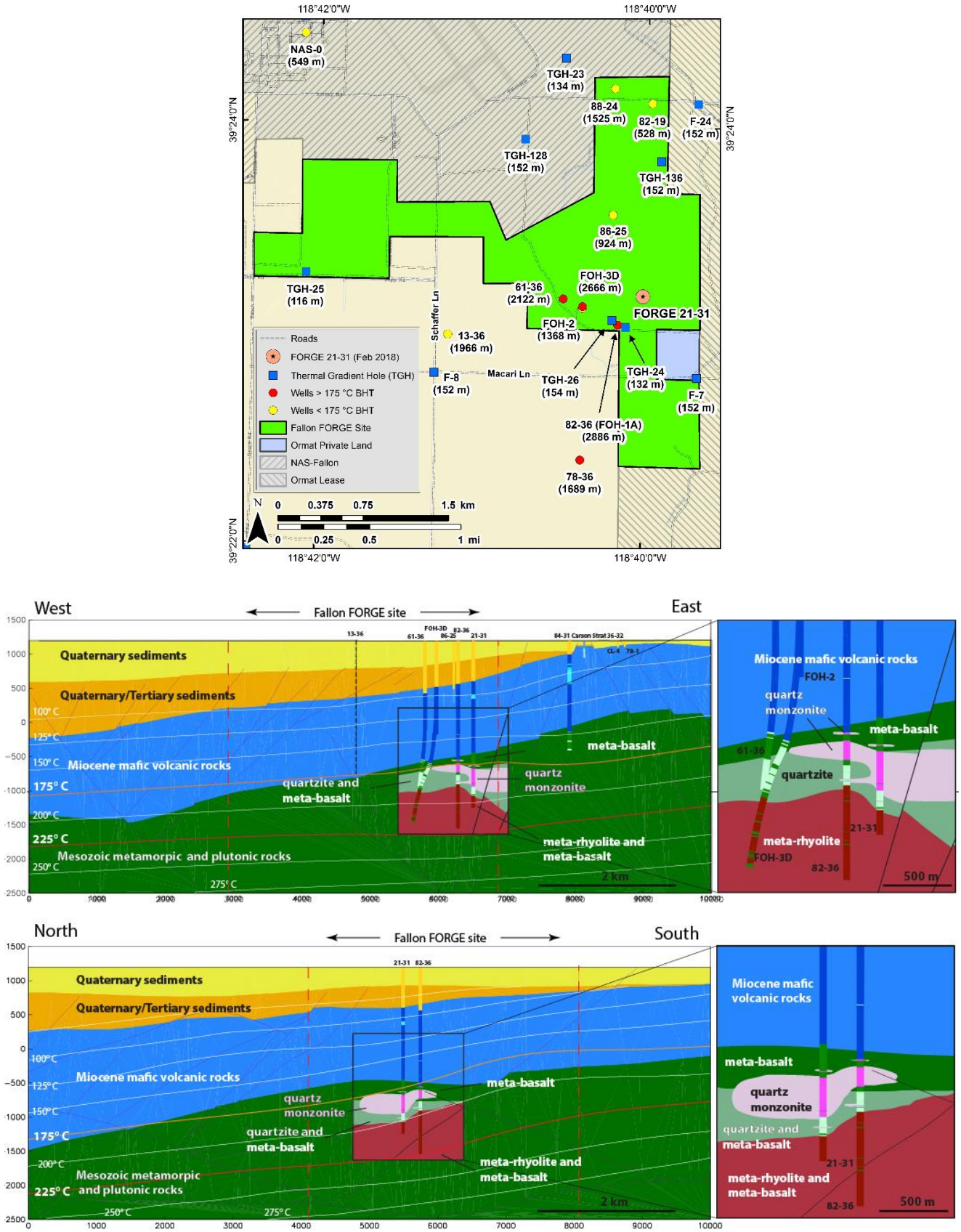

Figure 1: Well locations of the Fallon FORGE EGS site (top) and cross sections from site geologic model (bottom; sourced from Siler et al., 2018). This paper focuses on well 21-31.

An analysis of 13 geothermal wells, and 34 temperature gradient wells on the site and in the adjacent areas was conducted and was used to facilitate the development of a detailed geologic model (Figure 1, Blankenship and Siler, 2018). The primary lithologies encountered at the Fallon site in the basin fill are: a) Quaternary sediments, b) Quaternary-Tertiary sediments, c) Miocene mafic volcanic rocks primarily basaltic andesite, but also lithic tuff, andesite, rhyodacite, and volcanic breccia. The basin fill lithologies lie unconformably on top of Mesozoic basement consisting of: a) Mesozoic quartz monzonite, b) Mesozoic meta-basalt and meta-basaltic-andesite, c) Mesozoic quartzite with to a less extent phyllite, meta-basalt, and marble, d) Mesozoic meta-rhyolite with lesser meta-basalt. Proposed formations for EGS stimulation include the quartz monzonite, quartzite, or meta-rhyolite. The deepest wells in the site (61-36, 82-36, and FOH-3D) that terminate in Mesozoic basement at 2112-2886 m depth record maximum bottom hole temperatures of 194 to 214 ˚C (Blankenship, 2016, Siler et al., 2016).

Alteration studies of wells adjacent to 21-31 are previously reported by Jones and Moore (2013) using X-Ray Diffraction (XRD) and petrographic analysis, conducted during an earlier phase of geothermal exploration for conventional hydrothermal resources. They analyzed samples from wells FOH-3, 82-35, 61-36, 84-31, 99-24, FDU-2D and 18-5. They found alteration zones typical of many geothermal fields, which they grouped into three types: argillic, phyllic, and propylitic. The argillic zones were found primarily in the Quaternary sediments and consisted of abundant smectite. The phyllic zone was found primarily in the Miocene volcanic rocks consisting of veins filled with botryoidal quartz, chlorite, epidote, laumontite, and calcite with smectite overprinting. Propylitic alteration was found in the basement lithologies which included actinolite, epidote, adularia, and plagioclase overprinted by chlorite, illite, quartz, and calcite. The temperatures suggested by the alteration zones are <225 ˚C for argillic, 225 ˚C to 250 ˚C for phyllic, and >250 ˚C for propylitic. In addition, clay minerals are also temperature sensitive: in many high temperature geothermal systems, there is a low temperature (<180 ˚C) smectite zone, interlayered smectite-illite ± chlorite (180 ˚C – 225 ˚C) and finally illite and chlorite without smectite (above 225 ˚C) (Henley and Ellis, 1983, Reyes, 1990). Based on the mis-match between the observed well temperatures, and the higher temperatures implied by alteration, as well as the occurrence of smectite overprinting higher temperature alteration minerals, it was suggested that the higher temperature alteration zones represent prior (relict) hydrothermal activity, and the argillic alteration represents the present day thermal regime. This is consistent with the lack of hydrothermal manifestations found at the surface in the Fallon site, and wellbore temperature profiles that have primarily conductive heat flow characteristics and low permeability.

2.2 Infrared Spectroscopy

	Structure	Group	Example	VNIR Response	SWIR Response	LWIR Response
Silicates	Inosilicates	Amphibole	Actinolite	Non-diagnostic	Good	Good
		Pyroxene	Diopside	Good	Moderate	Good
	Cyclosilicates	Tourmaline	Dravite	Non-diagnostic	Good	Moderate
	Nesosilicates	Garnet	Andradite	Moderate	Non-diagnostic	Good
		Olivine	Forsterite	Good	Non-diagnostic	Good
		Zircon	Zircon	Good	Non-diagnostic	Non-diagnostic
	Sorosilicates	Epidote	Clinozoisite	Non-diagnostic	Good	Good
	Phyllosilicates	Mica	Muscovite	Non-diagnostic	Good	Moderate
		Chlorite	Clinochlore	Non-diagnostic	Good	Moderate
		Clay Minerals	Kaolinite	Non-diagnostic	Good	Moderate
			Illite	Non-diagnostic	Good	Moderate
	Tectosilicates	Feldspar	Orthoclase	Non-diagnostic	Non-diagnostic	Good
			Albite	Non-diagnostic	Non-diagnostic	Good
		Silica	Quartz	Non-diagnostic	Non-diagnostic	Good
Non-Silicates	Carbonates	Calcite		Non-diagnostic	Good	Good
		Dolomite		Non-diagnostic	Good	Good
	Hydroxides	Gibbsite		Non-diagnostic	Good	Moderate
	Sulphates	Alunite	Alunite	Non-diagnostic	Good	Moderate
			Barite	Non-diagnostic	Non-diagnostic	Good
	Borates		Borax	Non-diagnostic	Good	Uncertain
	Halides	Chlorides	Halite	Non-diagnostic	Moderate	Uncertain
	Phosphates	Apatite	Apatite	Moderate	Moderate	Good
			Amblygonite	Moderate	Good	Good
	Hydrocarbons		Bitumen	Non-diagnostic	Good	Uncertain
	Oxides		Hematite	Good	Non-diagnostic	Non-diagnostic
		Spinel	Magnetite	Non-diagnostic	Non-diagnostic	Non-diagnostic
	Sulphides		Pyrite	Non-diagnostic	Non-diagnostic	Non-diagnostic

Table 1: Capabilities of infrared reflectance spectroscopy for mineral identification for Very Near Infrared (VNIR), Short Wave Infrared (SWIR), and Long Wave Infrared (LWIR).

Infrared reflectance spectroscopy is an effective tool to collect mineralogical data, especially alteration mineralogy that is difficult to distinguish in hand sample or by petrographic methods. The technique does not require the lengthy sample preparation required for XRD analysis (Thompson 1999, Calvin and Pace 2016). Infrared absorption spectroscopy is useful for the analysis of geologic materials because many rock forming minerals display absorption features when interacting with electromagnetic radiation in the Very Near Infrared to Short Wave Infrared (VNIR-SWIR, 400-2500 nm) and Long Wave or Thermal Infrared (LWIR, 3-30 μm) wavelength ranges (Geiger, 2004). Absorption features in the VNIR-SWIR range are caused by either electronic processes, dependent on unfilled d orbitals, or vibrational processes, dependent on bonds in a crystal lattice (Clark, 1999). Molecules that show absorption features in the SWIR are O-H, C-O, cation-OH which can be used to identify amphiboles, carbonates, and phyllosilicates, including mica, chlorite, and smectite (Clark, 1999; Figure 2). The LWIR range is sensitive to the Si-O, P-O, and C-O bonds, and therefore is useful for identifying non-hydrated silicate minerals such as quartz or feldspar, carbonates, and phosphates (Salibury et al., 1991; Table 1). Spectral reference libraries, such as the U.S. Geological Survey, or the John Hopkins University are compared with sample spectra in order to identify minerals (Clark et al., 1990, Salisbury et al., 1991). In addition to mineral type, absorption bands are sensitive to crystal structure and subtle changes in chemistry (Clark, 1999).

Applied to geothermal drill core, infrared spectroscopy allows for the identification of alteration phases (Yang et al., 2000, 2001, Calvin and Pace, 2016). It is also useful for exploration and reservoir assessment in analyzing past temperatures, past fluid flow pathways, fluid acidity, and rock properties such as permeability, porosity, and strength (Browne, 1978, Reyes, 1990, Frolova et al., 2013, Wyering et al., 2014). Common minerals found in geothermal systems with SWIR responsive features include: aluminum phyllosilicates, such as smectites; the kaolinite group; the illite group; Fe-Mg phyllosilicates, such as chlorite group minerals; epidote group minerals; carbonate; and zeolites (Browne, 1978, Calvin and Pace, 2016; Figure 2). Examples of the application of infrared spectroscopy to conventional hydrothermal systems include a study by Yang et al. (2000, 2001) that investigated core from the Wairakei and Broadlands-Ohaaki geothermal fields using a portable SWIR spectrometer and characterized the alteration mineralogy and the zoning of alteration minerals. Calvin and Pace (2016) conducted a pilot study using a portable SWIR spectrometer on geothermal drill core, and identified alteration minerals and their zonation from point spectra measurements. This alteration information can inform understanding of past conditions within an EGS reservoir and can be used to predict the rock physical properties.

3. METHODS

3.1 Wireline Logs

The wireline log data used in this study can be accessed at the Geothermal Data Repository (Fallon, Nevada FORGE Well 21-31 Wireline Logs [data set]. Retrieved from http://gdr.openei.org/submissions/1068.) Wireline logs were collected February-March 2018 by Schlumberger. On February 25, 2018 four logs were collected within the 12.25 inch section of the well, from 90 to 1850 m (300 to 6068 ft) which included caliper logs, resistivity logs, Sonic Scanner, and triple combo. On 3/20, 3/24, 3/26, and 3/27 Fullbore Formation MicroImager (FMI), Pressure and Temperature (PT) survey, Sonic Scanner, triple combo, and UltraSonic Imager Tool (USIT) logs, and sidewall cores were collected within the 8.5 inch section of the well, from 1829 to 2480 m (6000-8139 ft). This paper focuses on the data from the Triple Combo logs (e.g. gamma ray, neutron porosity, density, and resistivity).

3.2 Hyperspectral Core Imaging System

Advances in high-resolution automated imaging spectroscopy are capable of collecting a spatially continuous hyperspectral data set from geothermal drill core that provides a new opportunity to evaluate spatial relationships of alteration minerals, and more thoroughly analyze cuttings samples within a smaller field of view than a portable spectrometer (Kraal et al., 2018). The instrument used in this study is the TerraCore™ hyperspectral core imaging system (HCIS) which operates via stationary line-scanning cameras, where the sample is placed on a table that is passed underneath the cameras at a controlled rate. This method allows for imaging the entire sample, such as a core box, with an average image collection speed of approximately 90 seconds. During each scan, a white and dark reference is collected for image calibration. The HCIS FENIX VNIR-SWIR camera utilizes 411 bands covering the VNIR-SWIR (463 nm – 2476 nm) with sampling approximately every 5 nm. The FENIX VNIR-SWIR, and OWL LWIR (7.6-11.9 μm) spectral cameras have a pixel size of 1.2 mm. In addition to a hyperspectral image, an RGB camera simultaneously creates a high-resolution (0.12 mm pixel size) image of the same drill core or sample.

The spectral data are converted to reflectance and the extraneous material such as the core box are masked to avoid mixed spectra from interfering with mineral identification. Spectra from the images are then separated into spectral endmembers using TerraCore's software. Each spectral endmember represents a unique spectral shape in a given image that may be composed of a single mineral or a mineral mixture. Spectral endmembers are then classified by mineral or mineral mixture through comparison with spectral library mineral standards, and images are made into mineral maps to demonstrate mineralogical variance within samples. The area of each endmember was calculated from the mineral maps, and plotted with depth to see how relative abundance of minerals changes with depth. Spectral data are also analyzed using feature extractions to create numerical data (spectral scalars).

Samples analyzed using the HCIS from well 21-31 include cuttings samples, and 'spot' or 'sidewall' cores collected in the basement section of the well. From well 21-31, 335 cuttings samples from depths 42 to 2,480 m (30-8,139 ft) were analyzed using the HCIS. Cuttings samples were imaged by spreading the cuttings sample out on a black background and imaging using the HCIS. Each cuttings sample represents a mixture of rock fragments from an approximate depth range of either 30 feet (for samples from less than 600 m depth) or 10 feet (samples greater than 600 m depth). Alternating cuttings intervals were imaged. In addition, 42 sidewall cores from the Mesozoic basement section were imaged, ranging in depth from 1,960 m to 2,470 m (6,430 to 8,104 ft). Sidewall cores were drilled horizontally into the wellbore and are either 1.5 or 0.9 inches in diameter, about 1-2.5 inches long, or are fragments only. Examples of sample types and mineral maps derived from hyperspectral imaging are shown in Figure 2.

The use of spectral scalars has been shown to provide additional mineralogical data in geothermal systems (Yang et al. 2000, 2001; Simpson and Rae, 2018). Spectral scalars are numerical data derived from spectra and include either feature wavelength locations (such as the wavelength location where a particular spectral feature is deepest, related to mineral structure) and feature depths (measure the 'strength' of the absorption feature, against background reflectance). Spectral scalars calculated for this study include the wavelength of the 2200 nm feature, which is related to Al-OH bond that varies depending on illite/muscovite composition, or by mineral, such as montmorillonite smectite (Pontual et al., 1997; Yang et al., 2011). The wavelength of the 2250 nm feature is related to Fe-OH bond, and gives information about the relative Fe/Mg composition of chlorite (Pontual et al., 1997). To find the depths of the smectite, illite/smectite, and illite zones, we analyzed the relative proportion of illite and smectite by the H_2O/Al-OH ratio, calculated from measuring the reflectance above 0 for both the 1900 nm feature and the 2200 nm feature. This ratio is based on the calculation used by Simpson and Rae (2018), which quantitatively estimated the relative proportions of illite/smectite from the 1900:2200 nm feature depth ratio based on calibrations with XRD data. Because we did not conduct XRD analysis on the entire depth range of well 21-31 we were not able to make the calibration necessary for a more quantitative result. However, the use of the spectral scalar ratio still provides relative abundance information. Chlorite spectral maturity was also calculated to measure the relative amounts of Fe-OH or Mg-OH absorption against H_2O absorption. Table 2 shows the scalars used in this study.

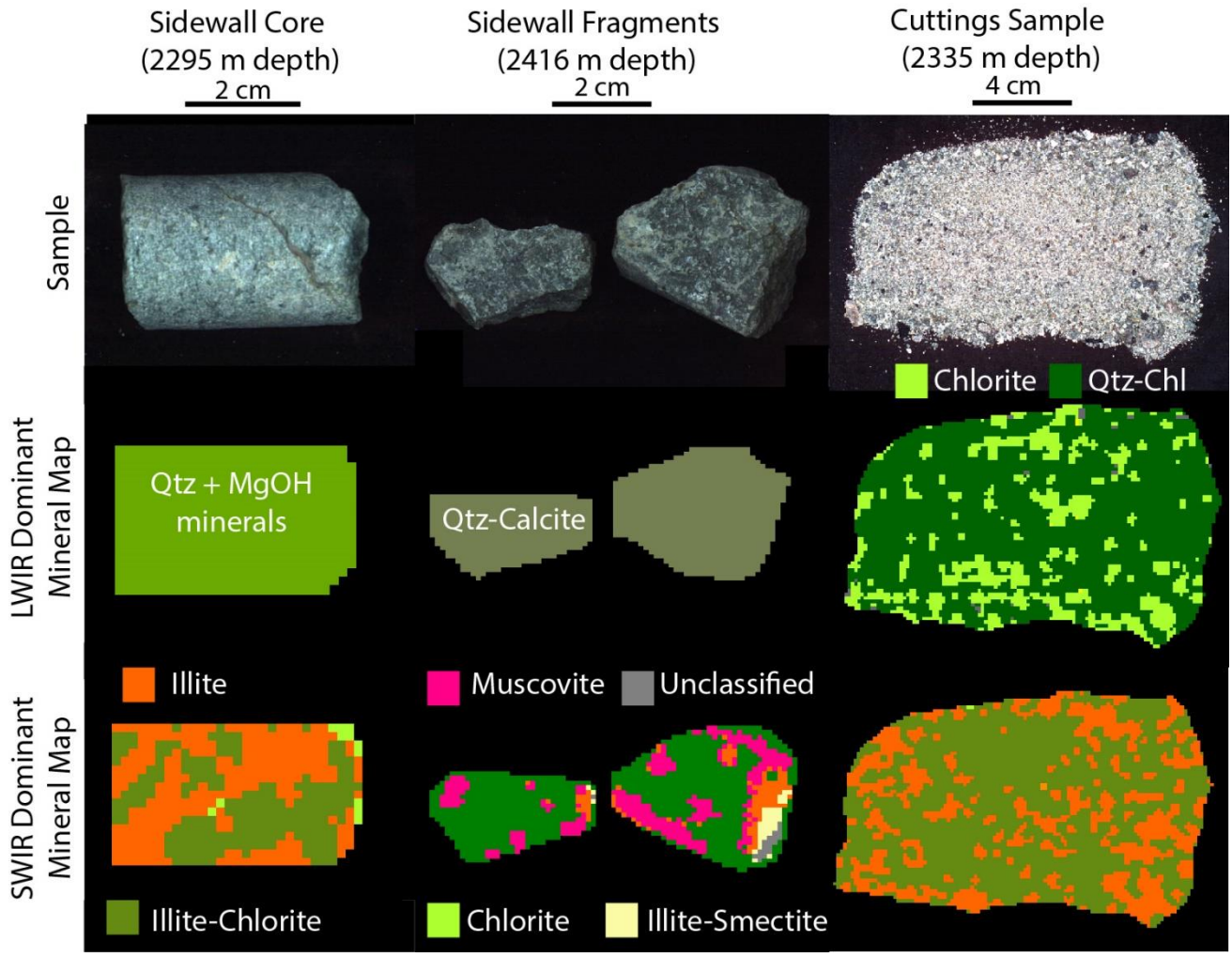

Figure 2: Examples of sample types and corresponding dominant mineral maps used in this study. Mineral maps of cuttings were used to create relative mineral abundance with depth logs, which we display in Figures 5, 6, and 7.

Scalar	Calculation	Description	Source
Illite Maturity	(1-D1800:2020)/ (1-D2180:2232)	Measures ratio between Al-OH absorption and H_2O absorption features related to amount of water in mineral structure compared to Al, can be used to estimate relative abundance of illite/smectite	Simpson and Rae, 2018
Chlorite Maturity	(D2300:2370+1.7*D2239:2277)/ (D1880:2020)	Measures chlorite maturity in low grade metamorphic environments	Douublier et al., 2010
Al-OH Wavelength	W2180:2232	This wavelength is related to illite composition and Al-OH mineral structure	Clark et al., 1990
Fe-OH Wavelength	W2239:2277	Wavelength related to chlorite composition	Pontual et al., 1997
LWIR Wavelength of highest absorption	W7600:11900	Tells the wavelength of the highest absorption across the LWIR measured	

Table 2: Spectral scalars calculated in this study. All scalars were calculated from hull quotient spectra. "Dxxxx:yyyy" refers to feature depth of largest feature in wavelength range xxxx to yyyy (nm). "Wuuuu:vvvv" refers to wavelength (nm) of deepest feature within wavelength range uuuu to vvvv.

3.3 Thin Section Analysis

Thin-sections were made from all 45 sidewall cores, as well as 20 cuttings samples spanning the Mesozoic basement section. Example thin sections for the primary lithologies observed in the Mesozoic basement are shown in Figure 3.

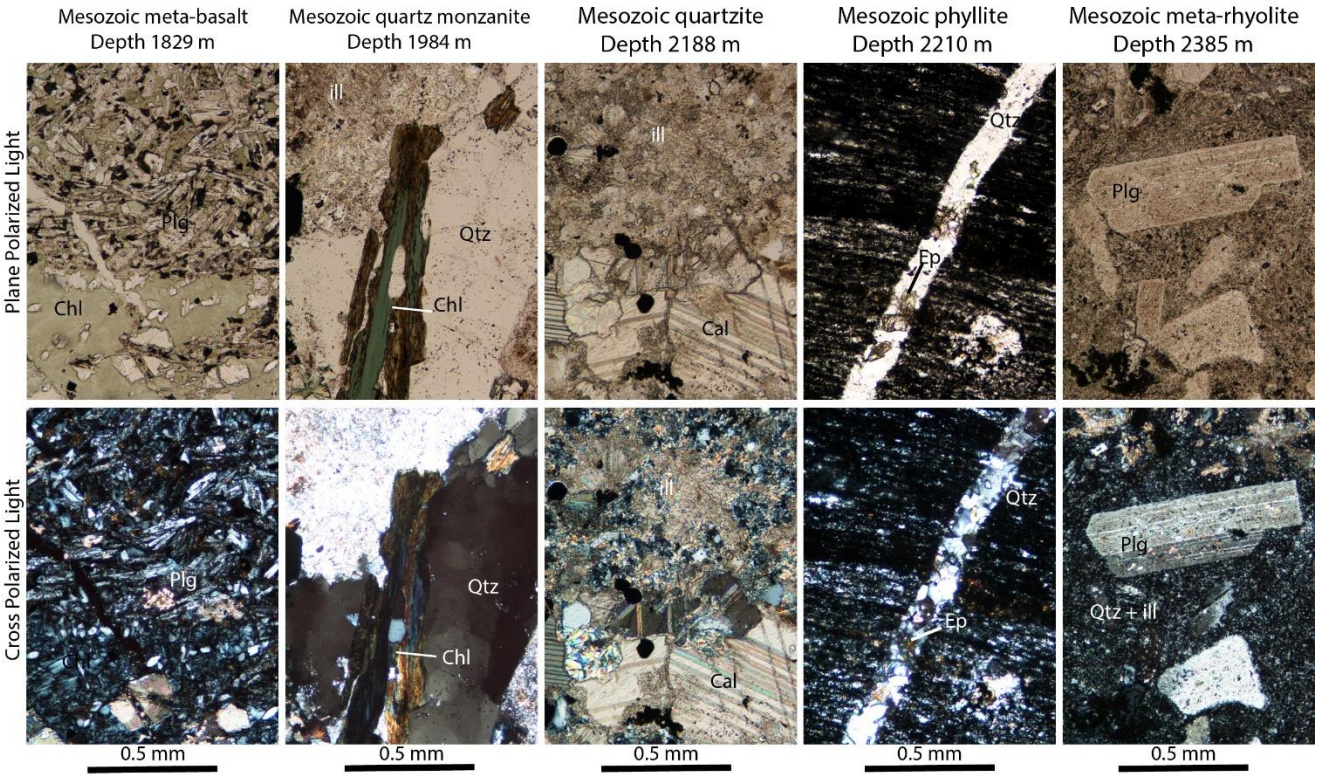

Figure 3: Thin sections from sidewall cores. XRD analysis was also performed on the samples displayed above (Table 3). Abbreviations: Chl: chlorite, Qtz: quartz, ill: illite, Cal: calcite, Ep: epidote, Plg: plagioclase.

3.4 X-Ray Diffraction

Whole rock XRD analyses were performed on 14 samples from the basement section of Fallon Well 21-31. The analyses were done at the Energy & Geoscience Institute at the University of Utah (Carlson and Jones, 2018). On two samples, the clay-sized-fraction was separated and also analyzed in addition to the bulk analysis. The methods performed are described by Moore and Reynolds (1997). The samples analyzed were all from the Mesozoic section of the well, four on sidewall cores from the Mesozoic meta-rhyolite section, five from sidewall cores from the Mesozoic meta-sedimentary/volcanic section, and three on sidewall cores samples from the Mesozoic quartz monzonite section, and two on cuttings samples from the Mesozoic meta-basalt unit. Results are shown in Figure 6. Samples from 1984 m (6510 ft) and 2423 m (7950 ft) had their clay-sized fractions analyzed separately as well.

4. RESULTS

4.1 Hyperspectral results

The primary minerals identified in the SWIR wavelengths from well 21-31 are montmorillonite smectite, saponite, chlorite, calcite, illite, epidote, and kaolinite (Figure 4, 6). The primary minerals identified in the LWIR are chlorite, quartz, feldspar, epidote and unidentified clay, Al-OH, and Mg-OH minerals (Figure 4, 6). Figure 4 shows the spectral endmembers classified by mineral or mineral mixture from the cuttings samples. Smectite is identified by large asymmetric absorption fields at 1400 nm (O-H bond) and 1900 nm (H_2O), as well as an absorption feature at 2200 nm (Al-OH) for montmorillonite and biedellite, and 2300 nm for saponite. Illite is characterized by sharper 1400 nm, 2200 nm, and 2350 nm absorption features, as well as a smaller 1900 nm feature than smectite. Muscovite was distinguished from illite by generally sharper features, a smaller 1900 nm feature, and an additional absorption feature at 2450 nm. Chlorite spectra is characterized by a boxy 1900 nm feature, a 2250 (Fe-OH) and 2350 features (Mg-OH). In our sample analysis, chlorite is most often observed mixed with illite or epidote, and this mixture creates an absorption triplet that varies in relative depth of absorption features. Similar absorption triplets of this composition are seen in Calvin and Pace, (2016), and Yang et al. (2000). LWIR is more difficult to interpret than SWIR because many combinations are non-unique. The quartz spectra were distinguished by a doublet between 8000 and 10000 nm, related to the Si-O-Si stretching vibrations. Chlorite LWIR is characterized by a large feature at 9600 nm.

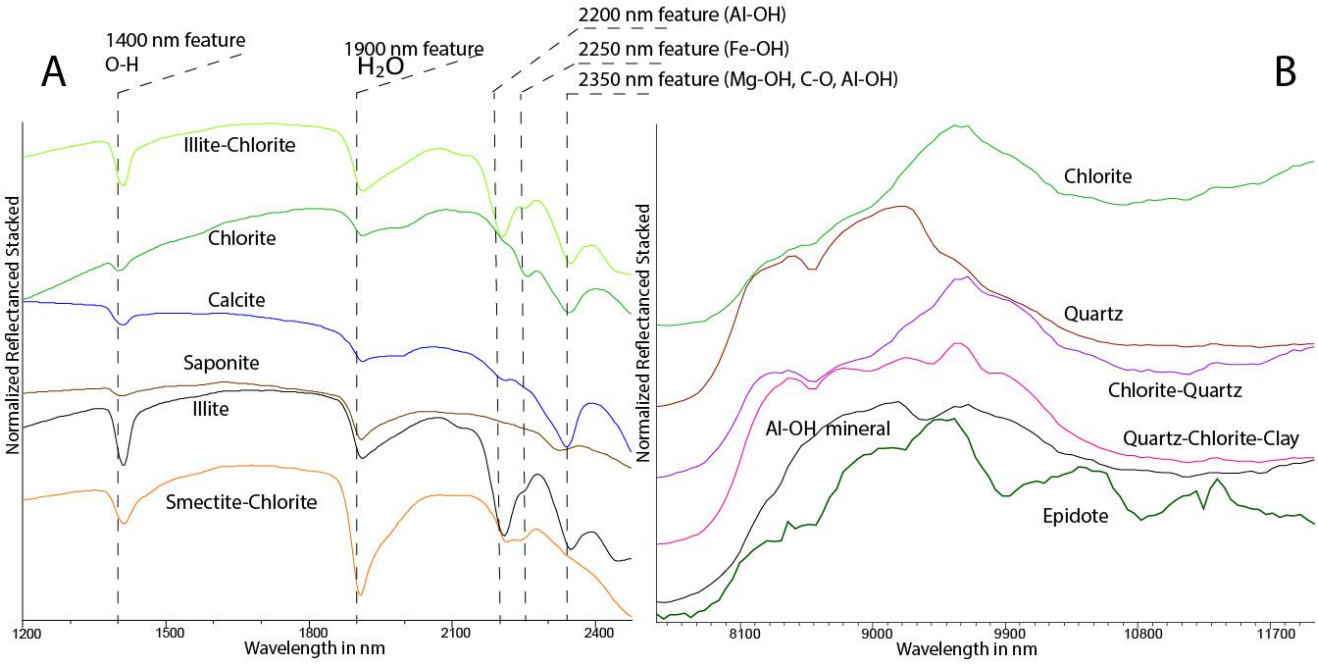

Figure 4: Spectral endmembers from well 21-31 cuttings. A: SWIR endmembers, B: LWIR endmembers. Each spectral endmember represents the average spectral shape for spectra classified as this endmember. Spectra are plotted as stacked normalized reflectance for clarity. Spectral classification written alongside spectra. Classification was based on the shape and location of absorption features through comparisons with spectral libraries, such as the USGS spectral library, and the JHU library (Clark et al. 1990, Salisbury et al., 1991). The location of various diagnostic absorption features are labeled in the SWIR.

In general, the major changes in mineralogy observed using hyperspectral imaging correlate with the boundaries of geologic formations in the well (Figure 5). The smectite-chlorite spectral endmember was the primary mineral observed in the quaternary sediments, although there are rare zones of abundant smectite-chlorite found within the Tertiary volcanic, Mesozoic meta-basalt, and at the bottom of the meta-quartz monzonite. Saponite is the most common mineral observed in the Tertiary volcanic units, although there are zones of chlorite observed within this unit. In both the quaternary sediments and the Tertiary volcanics, chlorite is the most common mineral observed in the LWIR. The meta-basalt unit is characterized in the SWIR by a mixture of saponite, chlorite, calcite, with some smectite and in the LWIR is much more quartz rich than the Tertiary basaltic-andesite, likely due to the increased chlorite alteration and quartz/calcite veining. The contact between basaltic andesite and Mesozoic meta-basalt is difficult to determine in both this data set and visual analysis of cuttings because the base of the Tertiary basaltic-andesite unit is also altered to chlorite and cut by later quartz and calcite veining, and is similar in composition. The quartz monzonite unit is characterized by illite, and illite-chlorite spectra in the cuttings SWIR, and quartz, then quartz-chlorite-clay spectra in the cuttings LWIR. In addition, analysis of spot cores observed muscovite, kaolinite, smectite, and feldspar in this unit. The Mesozoic meta-sedimentary/volcanic unit (2195-2298 m) shows much variability in spectra, which is expected from the heterogeneous lithology observed in cuttings and core. Primary spectra observed in this unit include chlorite, illite + chlorite, smectite, saponite in the SWIR, and a mix of quartz, chlorite, quartz + chlorite, and quartz + chlorite + clay spectra in the LWIR. In addition, spot core analysis also identified smectite, muscovite, feldspar, and epidote in this package. The meta-rhyolite unit is characterized by more illite spectra than the quartz monzonite, and more pure quartz spectra in the LWIR especially in the lower portions of this unit. The spot

core from the meta-rhyolite are composed of epidote, montmorillonite smectite, calcite, and feldspar in addition to the minerals observed in the cuttings samples, and muscovite is more common than observed in shallower units,.

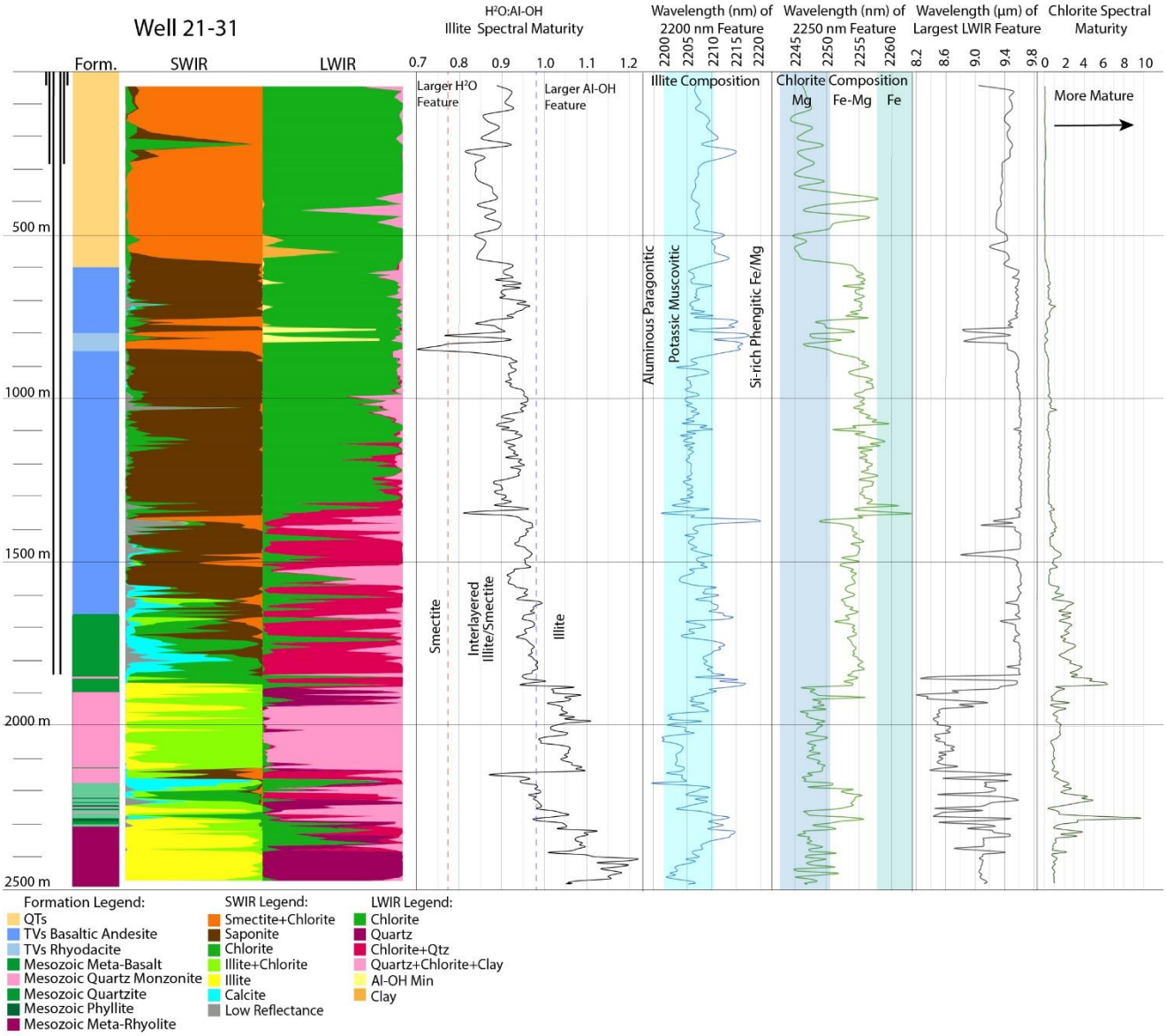

Figure 5: Well 21-31 lithology, cuttings hyperspectral interpretation, and spectral scalars with depth. Lithology designations from Fallon, Nevada FORGE Lithology Logs and Well 21-31 Drilling Data [data set]. http://gdr.openei.org/submissions/1027. For the SWIR and LWIR mineral logs, spectra from each sample interval were interpreted for dominant mineralogy, and plotted as a percent of the sample area with that mineral endmember spectra versus depth. For scalar descriptions see figure 4 and text. Scalars were calculated on hull corrected data for the entire sample image, and the average value for each sample is plotted above.

4.2 XRD Results

Minerals identified with XRD include illite/mica, chlorite, plagioclase, K-feldspar, quartz, magnetite, anhydrite, hematite, pyrite, epidote, and possibly trace sphalerite, interlayered chlorite/smectite, and smectite (Table 3). The Mesozoic-basalt unit XRD samples are primarily composed of plagioclase, quartz, and chlorite, with <10% K-feldspar and calcite, and trace magnetite and hematite. The Mesozoic quartz monzonite intrusion samples from the main intrusive body are composed primarily of plagioclase and quartz, with little or no K-feldspar. The dominant clay observed in these samples is illite/mica. Chlorite and calcite are also present. <1% pyrite is also found. The Mesozoic quartzite sample analyzed was primarily calcite, with some quartz, illite, chlorite, plagioclase, K-feldspar, and pyrite. The Mesozoic phyllite sample was primarily epidote, with approximately equal parts plagioclase, quartz, K-feldspar, some chlorite, and calcite, but did not contain illite/mica. The felsic intrusive rocks within the meta-sedimentary section are distinguished from the main quartz monzonite body by being illite/mica poor compared to the other felsic intrusive rocks, by the presence of epidote, and relatively more K-feldspar. The Mesozoic rhyolite unit is primarily quartz, illite/mica, and plagioclase feldspar, with some K-feldspar and calcite, but less chlorite.

5. DISCUSSION

5.1 Alteration Interpretation

The alteration in this study can be grouped into four zones: 1) Argillic A: montmorillonite + chlorite, found primarily in the Quaternary – Tertiary sedimentary package; 2) Argillic B: saponite + chlorite ± montmorillonite ± calcite ± illite, found primarily in the Tertiary basaltic-andesite section, and parts of the Mesozoic meta-basalt; 3) Sericitic/argillic: illite + chlorite ± kaolinite ± calcite, found primarily in the quartz monzonite intrusion unit; and 4) Propylitic: illite + chlorite + epidote ± muscovite ± calcite, found primarily in the Mesozoic quartzite package and the Mesozoic meta-rhyolite.

The distribution of clay minerals in well 21-31 in general imply increasing temperatures with depth. Smectites are the dominant clay minerals observed in depths 0-1,875 m (0-6,145 ft). Montmorillonite smectite, observed in the SWIR mixed with chlorite, is found most commonly in the Quarternary-Tertiary sediments, Tertiary volcanics, and Mesozoic meta-basalt, but is also abundant at 2,150 m near the transition between the Mesozoic quartz monzonite intrusion and Mesozoic sedimentary rocks, and in low abundance throughout the Mesozoic section (as deep as 2470 m). Montmorillonite is stable up to 180 ˚C, but is commonly found interlayered with illite up to 230 ˚C (Simmons et al., 1998; Reyes, 1990). Saponite is a common smectite mineral in geothermal systems, and has a wide thermal stability range of up to 300 ˚C (Eberl et al., 1978). The shallowest depth illite is observed in the well is at 1,300 m (Figure 5), but it does not become the most dominant clay mineral until 1,880 m depth, near the contact between the Mesozoic meta-basalt and quartz monzonite. Based on the high illite maturity calculated by the spectral scalars (Figure 5), the transition between the Mesozoic meta-basalt and the Mesozoic quartz monzonite intrusion at 1,893 m likely corresponds with the transition between interlayered illite/smectite and illite, which in active geothermal systems occurs at ~230 ˚C (Simmons and Browne, 2000). Muscovite is first observed in the SWIR image of the spot core at 1,961 m, but becomes more common at depths greater than 2,345 m within the Mesozoic meta-rhyolite unit. Based on the location of the 2200 nm feature, illite and muscovite compositions implied by the cuttings samples are primarily muscovitic (potassium rich) throughout the section, however some intervals show a more phengitic (Si rich) composition, particularly within the meta-basalt unit, the meta-sedimentary unit, and in some locations within the Tertiary basaltic-andesite (Figure 5). Montmorillonite has an absorption feature at 2208 nm, which overlaps with the wavelength range for the muscovitic illite observed, therefore this wavelength location is not useful for distinguishing between the smectite and illite zones.

Depth (m)	Lith	Smectite	Interlayered illite/smectite	Interlayered chlorite/smectite	Illite/Mica	Chlorite	Plagioclase	K-Feldspar	Quartz	Magnetite	Anhydrite	Calcite	Hematite	Sphalerite	Pyrite	Epidote
1707c	Mzb					19	43	8	23	tr		7	tr			
1829c	Mzb					21	42	10	18	1		7				
1961	Mzi				9	7	43	1	36			3			1	
1984	Mzi				11	3	54	2	27			3			tr	
2076	Mzi				9	3	68		17			3				
2166	Mzi	?		?	8	7	57	1	12		5	9			1	
2188	Mzq				22	7	8	2	17			40			5	
2210	Mzp					4	13	17	19			5		tr?		43
2237	Mzi		2				26	24	45			tr			tr	2
2252	Mzi				1	3	29	24	35			2				7
2295	Mzr		?		29	4	17	6	34			tr			tr	9
2385	Mzr		?		24	5	24	2	36			6			3	
2423	Mzr				33		1	2	63						tr	
2461	Mzr				19		12	13	56						tr	

Table 3: X-Ray Diffraction (XRD) analysis results for well 21-31 samples (Carlson and Jones, 2018). The c denotes that this was a cuttings sample, the rest are from sidewall cores. Mineral abundances are given in percent. Tr means trace amounts were found. Question marks indicate possible mineral constituents that are not confirmed. Lithology legend: Mzb is Mesozoic meta-basalt, Mzi is Mesozoic felsic intrusion, Mzq is Mesozoic quartzite, Mzp is Mesozoic phyllite, Mzr is Mesozoic meta-rhyolite.

Chlorite is found throughout the entire depth interval covered by well 21-31. Based on the cuttings sample SWIR scalar analysis, chlorite compositions are primarily Mg rich in the quaternary sediments, Fe-Mg in the Tertiary volcanic unit, become slightly more Mg rich in the meta-basalt, and are Mg rich in the quartz monzonite and meta-rhyolite, but more Fe rich in the meta-sedimentary zone (Figure 5).

Chlorite compositional changes appear primarily controlled by changes in lithology, rather than with depth. Chlorite spectral maturity is highest in the meta-basalt unit, and in some of the meta-sedimentary/basalt unit, particularly in areas where unmixed chlorite spectra was observed (Figure 5).

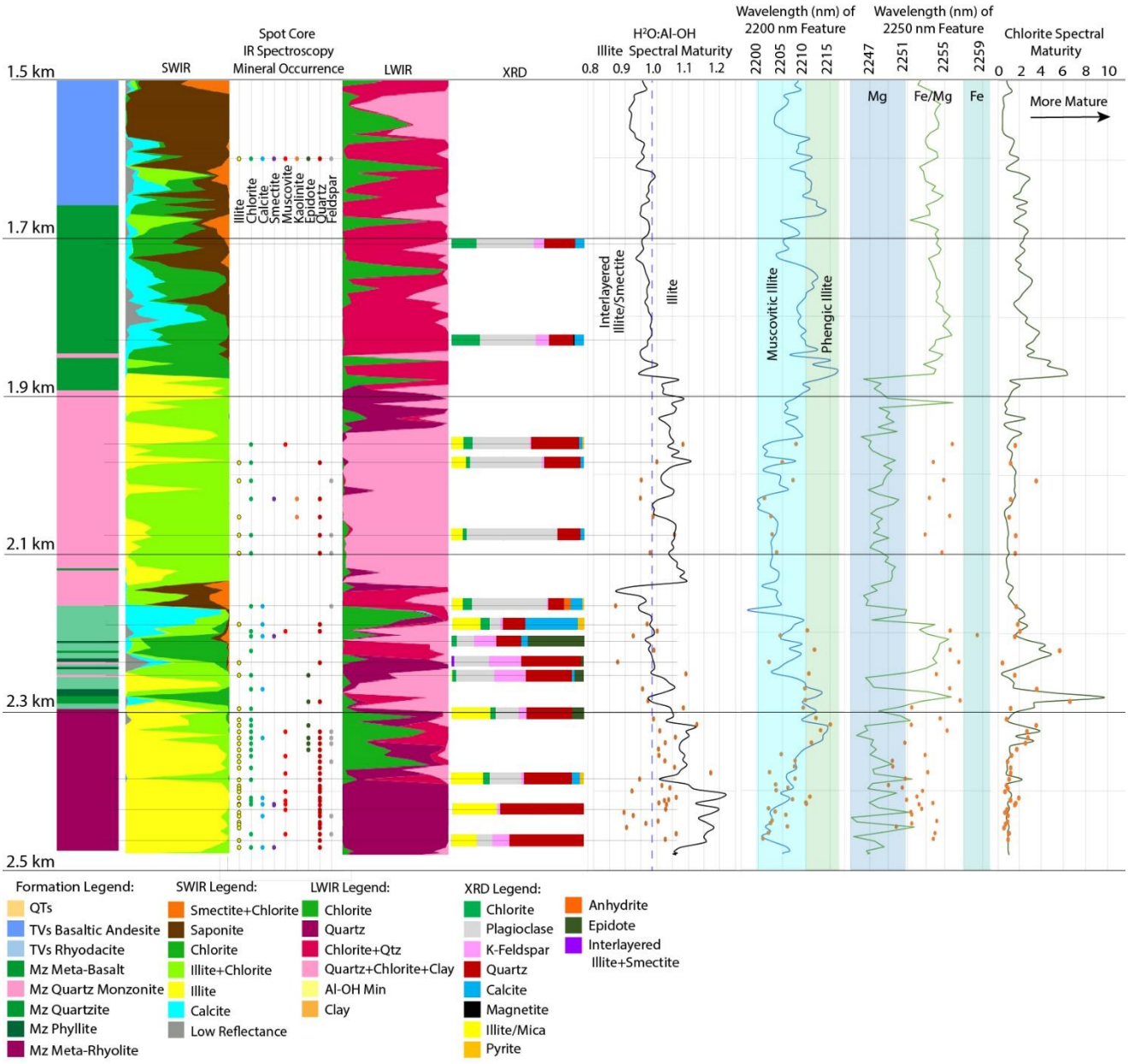

Figure 6: Mesozoic basement section cuttings and spot core hyperspectral and XRD analysis comparison. Orange dots in the spectral scalars represent average measurements from each spot core hyperspectral image.

Additional alteration minerals observed in well 21-31 include epidote, anhydrite, and kaolinite. Epidote is first observed at 2210 m in XRD analysis of spot core (Figure 6). Epidote forms in hydrothermal temperatures greater than 240 ˚C (Browne and Ellis, 1970). Anhydrite was observed at 2,166 m depth, and is typically formed at temperatures of greater than 180 ˚C (Reyes, 1990). Kaolinite was observed on the spot cores in SWIR at depths of 2,053 m (6,735 ft) which implies temperatures below 200 ˚C, and in hydrothermal systems is associated with more acidic, steam-heated waters rather than neutral chloride waters (Henley and Ellis, 1983, Reyes, 1990). Quartz and adularia were observed in veins as an alteration phase through the thin section analysis. Although LWIR spectroscopy was able to identify quartz and feldspar, we were not able to distinguish if they were primary or secondary minerals.

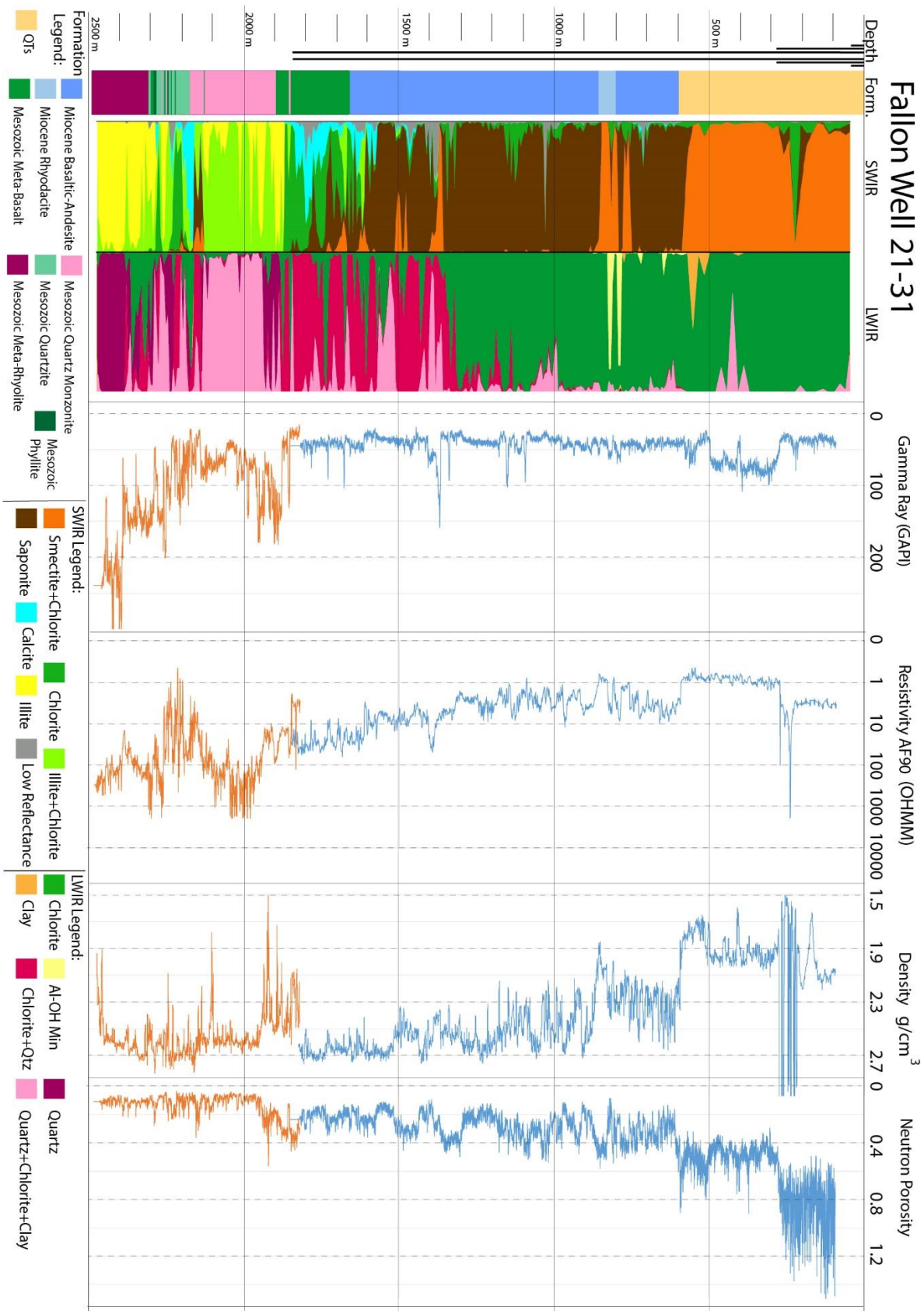

Figure 7: Well 21-31 selected triple combo wireline log data compared to lithology and hyperspectral cuttings data. Blue wireline data from the top section of the well, and orange from the basement section. Logs displayed are: GR, GR-STGC, RHOZ, RHOM, NPOR, and AF90.

Much of the alteration observed in the basement section of well 21-31 does not match the current thermal regime. Based on the temperatures measured for this depth interval in neighboring wells, temperatures are not interpreted to exceed 214 ˚C, which is considerably lower than temperatures required to form epidote (240 ˚C). The smectite alteration observed is more consistent with the current temperature regime within the well. This mismatch between the current temperatures and the temperature implied by the alteration minerals encountered in the well provides further proof that there is not an active hydrothermal system at this location. Hydrothermal systems bring higher temperature fluids to shallower depths and perturb the thermal regime, resulting in elevated temperatures relative to the background thermal regime. The overprinting of higher temperature alteration by lower temperature alteration in well 21-31 is in agreement with previous alteration studies in wells at the Fallon site (Jones and Moore, 2013).

5.2 Differences between Core and Cuttings analysis

The spot cores have better control on sample depth than cuttings because cuttings are formed at the bottom of the well and subsequently flushed up to the surface with circulating drilling fluid. Because of this, depth must be estimated based on return time of material from the bottom of the wellbore. Due to natural variation in densities of material and cuttings size, analysis of cuttings samples must take in account the variation in travel times of different portions of the material in one sample. With spot core, sample depths are more constrained. According to Hinz (2018, personal communication), cuttings sample depth estimates from well 21-31 typically appeared 10 meters (30 ft) above analogous spot core. Spot core lithology depths were chosen over depths estimated by cuttings samples for determination of formation boundaries in Figures 5, 6, and 7.

In general, both cuttings and core sample analysis found the dominant alteration mineralogy (illite, chlorite calcite, smectite, quartz) however there was more minerals observed in the spot cores (muscovite, epidote, kaolinite, feldspar) (Figure 6). The most likely explanations for discrepancies between hyperspectral analysis of core and cuttings samples are: 1) There is a tendency for certain minerals to be lost in the process from the bottom of the borehole, to being washed clean of drilling mud, before finally being analyzed; 2) cuttings samples contain a homogenized mixture of all the material, and therefore the more spectrally dominant minerals can override the less spectrally dominant minerals that may be present; 3) less common lithologies encountered in the well get mixed with more common lithologies, and therefore the minerals from the less common lithologies can be missed; 4) the mixing process leads to more mineral mixtures observed in spectra, which are more difficult to interpret (for example: it is harder to spectrally distinguish chlorite from epidote when mixed with clays and carbonates; 5) minerals without water in their structure may become hydrated during the drilling process when exposed to hot wet mud, (example: muscovite-illite); and 6) the analysis process for the cuttings versus the core varied slightly: for the cuttings, the entire borehole was analyzed to create spectral endmembers, while each spot core was analyzed individually, which likely affects the statistics used in the endmember creation algorithm.

There is also variation between cuttings and core samples in the spectral scalars observed (Figure 6). Variations in the illite spectral maturity are likely due to sample preparation. Many of the deeper spot cores were still wet from drilling, and the interference of this unbound water at the 1900 nm feature decreases the spectral maturity scalar value on these samples. However, it does not interfere with the 2200 nm feature, and therefore this feature appears consistent in both sample types.

5.3 Comparison with XRD results

In general, similar minerals were observed in both the XRD and IR spectroscopy (illite/muscovite, chlorite, calcite, smectite, epidote, quartz, feldspar) (Figure 9). XRD is able to identify minerals that do not have spectral responses, and therefore estimates the volume percent of all mineral constituents that are present in a sample (which infrared spectroscopy cannot). However, the methods described in this paper for HCIS cuttings analysis show one possible way to obtain relative mineral abundance information from hyperspectral imaging. These are not quantitative but still are useful for interpreting changes in mineralogy with depth within a well. In addition, the lack of sample preparation requirements, and speed of analysis allowed for higher spatial resolution investigation than commonly applied to alteration studies for geothermal reservoir characterization. Therefore, we believe the HCIS is a valuable tool to be used alongside XRD methods for analyzing core and cuttings sample for EGS site characterization.

5.4 Comparison with Wireline Logs

The Gamma ray logging measures the natural gamma radioactivity in rocks and is useful in correlating units between different wells and for providing additional information about the location of formation boundaries for various units. Gamma ray logs are expected to be highest in more felsic igneous rocks, and in sedimentary rocks, both which contain more radioactive elements such as potassium, isotopes from the uranium decay series, or the thorium decay series (Ellis and Singer, 2007). Minerals that typically contain abundant radioactive elements include potassium feldspars and clays such as illite, muscovite, glauconite, chlorite, montmorillonite, and kaolinite (Ellis and Singer, 2007). Gamma ray correlations with interpreted formation boundaries are observed in well 21-31. The most obvious is a sharp increase at 1855 meters and again at 1880 meters, corresponding with the location of the first narrow quartz-monzonite intrusion, and then the contact of the larger intrusive body in the well (Figure 7). Another possible correlation between hyperspectral data and the gamma ray log occurs at 1620 meters where the gamma ray log slightly increases, corresponding with an increase in the occurrence of illite in the well (observed as illite-chlorite in SWIR). This location may mark the beginning of the Mesozoic meta-basalt unit, which was difficult to distinguish from the altered lower part of the Tertiary basaltic andesite section. Gamma ray measurements are relatively higher in the smectite rich areas of the Tertiary section, such as at 1370 meters. These zones may indicate sedimentary interbeds within the basaltic andesite, or areas of higher alteration, both of which may increase radioactive element abundance relative to the more mafic volcanic rocks. We also note a possible correlation between gamma ray values and illite spectral maturity measurements; both generally increase with depth, and large positive and negative changes occur at similar depths (Figure 5, 7).

Density logs are measured using gamma ray absorption and give an estimate of the bulk density of the rock along the wellbore. In general, bulk density measurements were about 1.6-2.1 grams per cm^3 for the Quaternary-Tertiary sedimentary package, 2.1-2.8 g/cm^3 for the Tertiary basaltic andesite, 1.9-2.1 g/cm^3 for the Tertiary rhyodacite, 2.5-2.8 g/cm^3 for the Mesozoic meta-basalt unit, 2.1-2.7 g/cm^3 in the quart-monzonite unit, and about 2.5-2.8 g/cm^3 for much of the meta-sedimentary and meta-rhyolite units, however there are zones with much lower densities (e.g., 1.8 g/cm^3 at 2,100 m and 2,450 m) (Figure 7).

Neutron porosity logs measure neutrons which are useful for porosity estimates because hydrogen in formations is efficient at slowing down neutrons (Ellis and Singer, 2007). The primary source of hydrogen within these formations are water, which are often found in pore spaces and therefore useful for porosity estimation. However, the method is also sensitive to hydrogen within hydrous minerals that can result in neutron porosity values higher than true porosity. The most obvious correlation between the neutron porosity log and lithology occurs at 700 meters where there is a sharp decrease in neutron porosity, and the contact between the Quaternary-Tertiary sediments, and the Tertiary basaltic andesite (Figure 7). Care must be taken in interpreting neutron density logs because these logs are sensitive to borehole effects such as caving and wash-out within the well.

Within the Quaternary sediments, resistivity values range from 0.5-1.5 ohm meters, are typically between 1-15 ohm meters in the Tertiary volcanic section, 10-100 ohm meters in the meta-basalt, 100-1500 ohm meters in the quartz monzonite intrusion, 0.5-100 ohm meters in the Quaternary sediment section, and 50-1200 ohm meters in the meta-rhyolite (Figure 7). This resistivity pattern is similar to what is seen in many active geothermal systems (for example, Ussher et al., 2000; Arnason et al., 2008) where resistivity is controlled by the hydrothermal alteration in the well. In active hydrothermal systems, resistivity is lowest in smectite rich sediments and clay caps, and highest in high temperature illite + chlorite type alteration zones found in the deeper portions of geothermal upflow. Well 21-31 is similarly structured because resistivity is lowest in the smectite rich Quaternary sediments, and highest in the high temperature, propylitic type alteration zones in the Mesozoic basement.

6. CONCLUSION

Our results demonstrate the usefulness of hyperspectral imaging for EGS reservoir and lithological characterization. Hyperspectral imaging of core and cuttings samples provides a high spatial resolution dataset that is useful to analyze the distribution of alteration mineralogy in wells. In the Fallon FORGE well 21-31, the distribution of alteration minerals includes four primary zones: 1) montmorillonite smectite + chlorite alteration in the Quaternary basin infill section, 2) saponite as the dominant smectite mineral within the Tertiary volcanic section, with some chlorite, calcite and montmorillonite, 3) illite + chlorite alteration with some muscovite and calcite, in the Mesozoic sections with possible smectite overprinting in some areas, and 4) illite, chlorite, and epidote alteration with muscovite, calcite, and smectite overprinting in the Mesozoic meta-sedimentary/volcanic package and the meta-rhyolite unit. This zonation represents temperatures higher than currently observed in this well, therefore it is likely a relic of past hydrothermal alteration. The spectral data derived from the samples alongside wireline logs was useful for analysis of formation boundaries within the well. Spot cores analysis hyperspectral analysis provided more mineralogical information than cuttings analysis alone. Future work planned will integrate this data with wireline logs and hyperspectral measurements from other wells from the Fallon site to better constrain basement lithology and to further distinguish mineralogy patterns that represent current (and relict) geothermal activity within the system.

ACKNOWLEDGMENTS

New data acquisition in the Fallon FORGE well 21-31 was funded by a US Department of Energy grant EE007160 awarded to Sandia National Laboratories, with a sub-contract to the University of Nevada, Reno. We wish to thank the entire Fallon FORGE team, including Nicholas Hinz, Drew Siler, Logan Hackett, Wendy Calvin, and James Faulds. We would also like to thank Jason Craig and Elijah Mlawsky at the Great Basin Center for Geothermal Energy/NBMG for assistance with data compilation and visualization. We would also like to thank Dave Browning and Paul Linton from TerraCore for their help in imaging the samples from well 21-31. Christopher Carlson and Clay Jones at Energy & Geoscience Institute conducted the XRD analysis.

REFERENCES

Árnason, K., Karlsdóttir, R., Eysteinsson, H., Flóvenz, Ó. G., & Gudlaugsson, S. T. (2000, May). The resistivity structure of high-temperature geothermal systems in Iceland. In *Proceedings of the World Geothermal Congress 2000, Kyushu-Tohoku, Japan* (pp. 923-928).

Browne, P. R. L. (1978). Hydrothermal alteration in active geothermal fields. *Annual review of earth and planetary sciences*, *6*(1), 229-248.

Browne, P.R.L., & Ellis, A.J. (1970). The Ohaki-Broadlands hydrothermal area, New Zealand; mineralogy and related geochemistry. *American Journal of Science*, *269*(2), 97-131.

Blankenship, D. (2016). Fallon FORGE Well Temperature Data [digital data set]. Sandia National Laboratories. Retrieved from http://gdr.openei.org/submissions/783.

Blankenship, D., & Siler, D. (2018). Fallon, Nevada FORGE 3D Geologic Model (No. 1014). DOE Geothermal Data Repository; Sandia National Laboratories. Retrieved from Retrieved from http://gdr.openei.org/submissions/1014.

Carlson, C.T., and Jones, C.G. (2018). X-ray Diffraction Analyses of 14 samples from well-21-31: Fallon, Nevada. Report prepared for University of Nevada, Reno.

Clark, R. N. (1999). Spectroscopy of rocks and minerals, and principles of spectroscopy. *Manual of remote sensing*, *3*(3-58), 2-2.

Clark, R.N., King, T.V.V., Klejwa, M., and Swayze, G.A. (1990). High Spectral Resolution Reflectance Spectroscopy of Minerals, *J. Geophysical Research*, vol. 95, pp. 12653—12680.

Doublier, M. P., Roache, A., & Potel, S. (2010). *Application of SWIR spectroscopy in very low-grade metamorphic environments: a comparison with XRD methods* (p. 61). Geological Survey of Western Australia.

Eberl, D. D., Whitney, G., & Khoury, H. (1978). Hydrothermal reactivity of smectite. *American Mineralogist*, *63*(3-4), 401-409.

Ellis, D. V., & Singer, J. M. (2007). *Well logging for earth scientists* (Vol. 692). Dordrecht: Springer.

Faulds, J. E., Hinz, N. H., Siler, D. L., Glen, J. M. G., Fortuna, M. A., Queen, J.H., Blake, K., and Fallon FORGE team, (2018), Update on the Stratigraphic and Structural Framework of the Proposed Fallon FORGE Site, Nevada. *GRC Transactions 42.* p.1026-1046.

Frolova, J., Ladygin, V., Rychagov, S., & Zukhubaya, D. (2014). Effects of hydrothermal alterations on physical and mechanical properties of rocks in the Kuril–Kamchatka island arc. *Engineering Geology*, *183*, 80-95.

Geiger, C. A., Beran, A., & Libowitzky, E. (2004). *An introduction to spectroscopic methods in the mineral sciences and geochemistry*. na.

Henley, R. W., & Ellis, A. J. (1983). Geothermal systems ancient and modern: a geochemical review. *Earth-science reviews*, *19*(1), 1-50.

Hinz, N.H., Faulds, J. E., Siler, D. L., Tobin, B., Blake, K., Tiedeman, A., Sabin, A., Blankenship, D., Kennedy, M., Rhodes, G., Nordquist, J., Hickman, S., Glen, J., et al. (2016). Stratigraphic and Structural Framework of the Proposed Fallon FORGE site, Nevada. PROCEEDINGS, 41st Workshop on Geothermal Reservoir Engineering: Stanford University, February 22-24 2016.

Kraal, K. O., Ayling, B., Calvin, W., & Browning, D., (2018), Comparison of a Portable Field Spectrometer and Automated Imaging on Geothermal Drill Core: A Pilot Study. *GRC Transactions* Vol. 42, 1327-1339.

Mielke, P., Nehler, M., Bignall, G., & Sass, I. (2015). Thermo-physical rock properties and the impact of advancing hydrothermal alteration—A case study from the Tauhara geothermal field, New Zealand. *Journal of Volcanology and Geothermal Research*, *301*, 14-28.

Moore, D. M., & Reynolds, R. C. (1989). *X-ray Diffraction and the Identification and Analysis of Clay Minerals* (Vol. 322, p. 321). Oxford: Oxford university press.

Pontual, S., Merry, N., & Gamson, P., (1997), Spectral interpretation field manual: Ausspec International Pty Ltd, Kew, Victoria 3101, Australia, Spectral Analysis Guides for Mineral Exploration G-Mex Version 1.0, 169.

Reyes, A. G. (1990). Petrology of Philippine geothermal systems and the application of alteration mineralogy to their assessment. *Journal of Volcanology and Geothermal Research*, *43*(1-4), 279-309.

Salisbury, J. W., Walter, L. S., Vergo, N., & D'Aria, D. (1991). Infrared (2.5-25 μm) Spectra of Minerals. The Johns Hopkins University Press. Baltimore and London.

Siler, D. L., Hinz, N. H., Faulds, J. E., Tobin, B., Blake, K., Tiedeman, A., Sabin, A., Lazaro, M., Blankenship, D., Kennedy, M., Rhodes, G., Dordquist, J.,, Hickman, S., Glen, J., Williams, C., Robertson-Tait, A., Calvin, W., & Pettitt, W. (2016). The geologic framework of the Fallon FORGE site. *Geothermal Resources Council Transactions*, 40, 573-584.

Siler, D. L., Hinz, N. H., Faulds, J. E., Ayling, B., Blake, K., Tiedeman, A., Sabin, A., Blankenship, B., Kennedy, M., Rhodes, G., Sophy, M. J., Glen, J. M. G., Phelps, G. A., Foruna, M., Queen, J., & Witter, J. B. (2018). The geologic and structural framework of the Fallon FORGE site. In: Proceedings of the 43rd Workshop on Geothermal Reservoir Engineering, Stanford University, February 12-14, 2018.

Simmons, S. F., Browne, P. R. L., Arehart, G. B., & Hulston, J. R. (1998). Illite, illite-smectite and smectite occurrences in the Broadlands-Ohaaki geothermal system and their implications for clay mineral geothermometry. *Water Rock Interaction*, 9, 691-694.

Simmons, S. F., & Browne, P. R. (2000). Hydrothermal minerals and precious metals in the Broadlands-Ohaaki geothermal system: Implications for understanding low-sulfidation epithermal environments. *Economic Geology*, *95*(5), 971-999.

Simpson, M. P., & Rae, A. J. (2018). Short-wave infrared (SWIR) reflectance spectrometric characterisation of clays from geothermal systems of the Taupō Volcanic Zone, New Zealand. *Geothermics*, *73*, 74-90.

Thompson, A. J. (1999). Alteration mapping in exploration: Application of short wave infrared (SWIR) spectroscopy. *Econ. Geol. Newsl.*, *30*, 13.

Ussher, G., Harvey, C., Johnstone, R., & Anderson, E. (2000, May). Understanding the resistivities observed in geothermal systems. In *proceedings world geothermal congress* (pp. 1915-1920).

Wyering, L. D., Villeneuve, M. C., Wallis, I. C., Siratovich, P. A., Kennedy, B. M., Gravley, D. M., & Cant, J. L. (2014). Mechanical and physical properties of hydrothermally altered rocks, Taupo Volcanic Zone, New Zealand. *Journal of Volcanology and Geothermal Research*, *288*, 76-93.

Yang, K., Huntington, J.F., Browne, P.R.L., & Ma, C.A. (2000). An infrared spectral reflectance study of hydrothermal alteration minerals from the Te Mihi sector of the Wairakei geothermal system, New Zealand, *Geothermics*, 29(3), 377-392.

Yang, K., Browne, P. R. L., Huntington, J. F., & Walshe, J.L. (2001). Characterising the hydrothermal alteration of the Broadlands-Ohaaki geothermal system, New Zealand, using short-wave infrared spectroscopy, *Journal of Volcanology and Geothermal Research*, 106(1-2), 53-65.

Yang, K., Huntington, J. F., Gemmell, J. B., & Scott, K. M. (2011). Variations in composition and abundance of white mica in the hydrothermal alteration system at Hellyer, Tasmania, as revealed by infrared reflectance spectroscopy. *Journal of Geochemical Exploration*, 108(2), 143-156.